A Wideband and Low-Loss Spatial Power Combining Module for mm-Wave High-Power Amplifiers

Citation for the original published paper (version of record):
Roev, A., Taghikhani, P., Maaskant, R. et al (2020)
A Wideband and Low-Loss Spatial Power Combining Module for mm-Wave High-Power Amplifiers
IEEE Access, 8: 194858-194867
http://dx.doi.org/10.1109/ACCESS.2020.3033623

IEEE Access
Multidisciplinary | Rapid Review | Open Access Journal

Received October 1, 2020, accepted October 18, 2020, date of publication October 26, 2020, date of current version November 6, 2020.

Digital Object Identifier 10.1109/ACCESS.2020.3033623

A Wideband and Low-Loss Spatial Power Combining Module for mm-Wave High-Power Amplifiers

ARTEM ROEV[1,2], (Member, IEEE), PARASTOO TAGHIKHANI[1], ROB MAASKANT[1,2], (Senior Member, IEEE), CHRISTIAN FAGER[1], (Senior Member, IEEE), AND MARIANNA V. IVASHINA[1], (Senior Member, IEEE)

[1]Department of Electrical Engineering, Chalmers University of Technology, 41296 Gothenburg, Sweden
[2]Department of Electrical Engineering, Eindhoven University of Technology, 5612 Eindhoven, The Netherlands

Corresponding author: Artem Roev (roev@chalmers.se)

This work is a part of the Silicon-based Ka-band massive MIMO antenna systems for new telecommunication services (SILIKA) project, funded by the European Union's Horizon 2020 research and innovation program under the Marie Skłodowska Curie grant agreement #721732.

ABSTRACT We present a low-loss power combiner, providing a highly integrated interface from an array of mm-wave power amplifiers (PAs) to a single standard rectangular waveguide (WG). The PAs are connected to an array of parallel and strongly coupled microstrip lines that excite a substrate integrated waveguide (SIW) based cavity. The spatially distributed modes then couple from the cavity to the rectangular WG mode through an etched aperture and two stepped ridges embedded in the WG flange. A new co-design procedure for the PA-integrated power combining module is presented that targets optimal system-level performance: output power, efficiency, linearity. A commercial SiGe quad-channel configurable transmitter and a standard gain horn antenna were interfaced to both ends of this module to experimentally demonstrate the proposed power combining concept. Since the combiner input ports are non-isolated, we have investigated the effects of mutual coupling on the transmitter performance by using a realistic PA model. This study has shown acceptable relative phase and amplitude differences between the PAs, *i.e.* within $\pm 15^\circ$ and ± 1 dB. The increase of generated output power with respect to a single PA at the 1-dB compression point remains virtually constant (5.5 dB) over a 42% bandwidth. The performed statistical active load variation indicates that the interaction between the PAs through the combiner has negligible effect on the overall linearity. Furthermore, the antenna pattern measured with this combiner shows negligible deformation due to non-identical PAs. This represents experimental prove-of-concept of the proposed spatial power combining module, which can be suitable for applications in MIMO array transmitters with potentially coupled array channels.

INDEX TERMS Antenna feed, array amplifiers, integration, MMIC, mode converter, spatial power combining.

I. INTRODUCTION

Highly integrated millimeter-wave transceivers with high output power and efficiency are of high demand for the next-generation wireless communication systems, imaging, and radar applications. Although III-V compound semiconductors are traditionally used for implementing the mm-wave power amplifiers, silicon is becoming more favorable due to its low cost and high integration capability [1]. However, the typical RF power that needs to be delivered by power amplifiers (PAs) in emerging applications is beyond the current state-of-the-art of silicon devices due to their relatively low breakdown voltage [2]. This problem can be overcome by combining signals from multiple PAs into a single radiating antenna element. However, this approach is not well-suited for IC solutions, since an on-chip combiner as well as an

The associate editor coordinating the review of this manuscript and approving it for publication was Jing Xia.

antenna and its interconnecting transition should be low-loss [3]–[6]. Moreover, losses in conventional circuit power combiners exacerbate if the number of channels increases [7], [8]. This fact limits the feasible combined output power and reduces efficiency. Table 1, which presents state of the art mm-wave integrated power combiners, exemplifies this effect for two CMOS-based combiners with 2 and 4 channels [8]–[10]. Another challenge is the integration with antenna elements, which are comparable in size to ICs at these frequencies [11]–[13].

TABLE 1. Comparison between state-of-the-art PA power combining solutions and the proposed design.

Reference	Number of channels	Freq, [GHz]	Bandwidth, [%]	Losses, [dB]
CMOS on-chip [8]	2	22-26	17	1.4
CMOS on-chip [9]	2	16-27	51	1.0
CMOS on-chip [10]	2	30-40	29	1.7
CMOS on-chip [8]	4	22-26	17	2.4
[this work]	4	24-38	42	0.3
[this work]	8	25-36	37	0.4

A possible solution towards the efficient wide band high power silicon-based transmitters at mm-wave frequencies is the recently proposed multi-channel transition with spatial power combining functionality [14], where an array of strongly-coupled microstrip lines (MLs) interface a single substrate integrated waveguide (SIW). The corresponding back-to-back configuration is a passive structure, hence, the effects of imperfect PAs on the radiation performance of an interconnected antenna element remain to be studied. This study is important to conduct because the MLs are not isolated (−8 dB). The PAs will therefore couple via the common SIW structure. In turn, the input ML active impedances change with the ML excitation. These active input impedances are the load impedances presented to interconnected PAs. The PA output power, efficiency, and non-linear distortion are highly dependent on the load impedance [15]. Consequently, the combined output power is affected by unequal PA signals; any deviation from the optimum PA load impedance leads to an output power and efficiency reduction [16].

Given the above motivation, the novel contributions of the current work are: (i) *a new design procedure* of the spatial power combiner in the presence of the critical effects of power amplifiers in linear and non-linear regimes; (ii) *experimental proof-of-concept* using a commercially available multi-channel PA IC. The key performance metrics are the combined output power, power efficiency, linearity, impedance matching and radiation pattern stability due to unequal PA input signals. This analysis approach allows to determine the requirements for the multi-channel transmitter gain spread in conjunction with the power combining module.

II. DESIGN OF THE POWER COMBINING MODULE INCLUDING THE EFFECTS OF PAs

Figure 1 shows a detailed model of the designed power combining module, which employs the spatially distributed excitation of the SIW-based cavity modes by an array of, in this case, four coupled MLs. A conventional waveguide interface was used as an output port to demonstrate the power combining performance and to measure the antenna pattern degradation of a standard gain horn in the presence of imperfect PAs and manufacturing tolerances. Furthermore, to integrate a WG interface, the design concept of the 90° bent interface between an SIW-based cavity with etched aperture and a stepped ridge WG has been employed [17]. However, instead of using the relatively bulky and long multi-section SIW in [17], the desired multi-mode field distribution in the relatively wide SIW cavity is in this case directly created by an array of coupled MLs [14]. The direct multi-mode excitation allows to reduce the size of the transition and hence the losses in comparison with [17]. The consequence is that our transition becomes inseparable and, therefore, must be designed and characterized as a single integrated multi-port unit. In contrast to the previous back-to-back design [14], where four quasi-TEM modes are matched to a single TE_{10} mode (See Fig. 2 (a)), the present structure has been optimized to directly match the over-moded cavity with an open aperture, as shown in Figure 2 (b). In this case, the electric field of the resonant cavity mode is concentrated near the bottom orthogonal ridge and is coupled through the

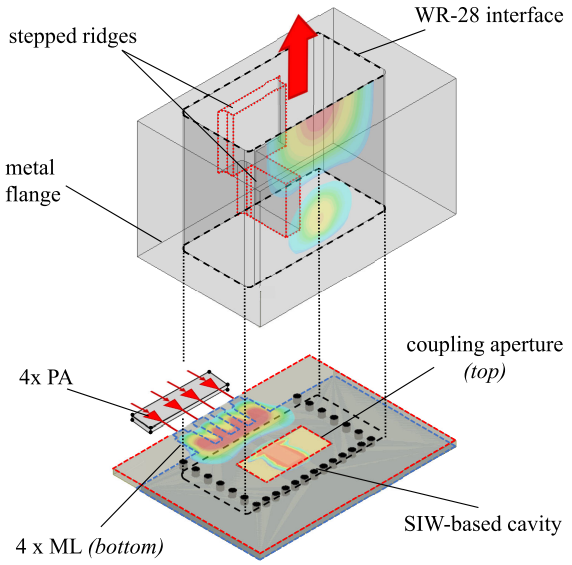

FIGURE 1. A detailed model of the proposed spatial power combining module. The PAs are interfaced to an SIW-based cavity with a coupling aperture through 4 spatially distributed microstrip lines (MLs) located on the bottom layer. The electric field of the resonant cavity mode is concentrated near the bottom orthogonal ridge and subsequently coupled through the etched rectangular aperture into the metal WR-28 flange with stepped ridges. The TE_{10} mode propagation inside the WG and direct coupling to the array of MLs are illustrated.

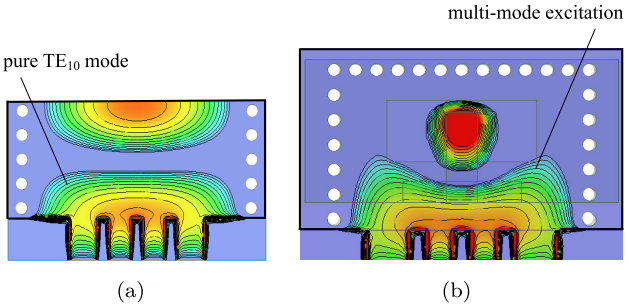

FIGURE 2. Magnitude of the E-field distribution at 30 GHz inside: (a) a single-mode SIW excited by an array of MLs [14]; (b) over-moded cavity with the open aperture excited by an array of ML.

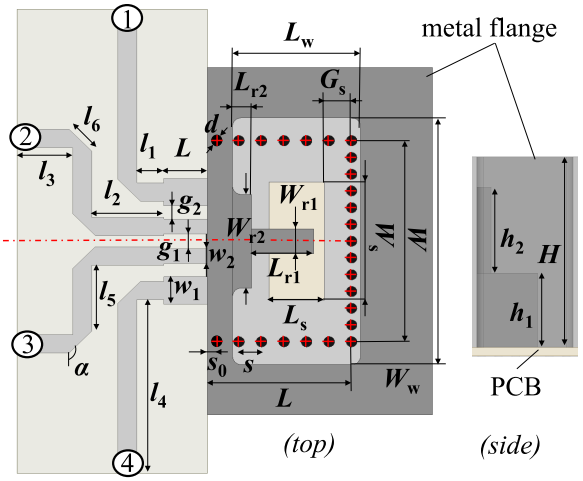

FIGURE 3. The geometry of proposed DUT including bent divergent routing lines to connectors.

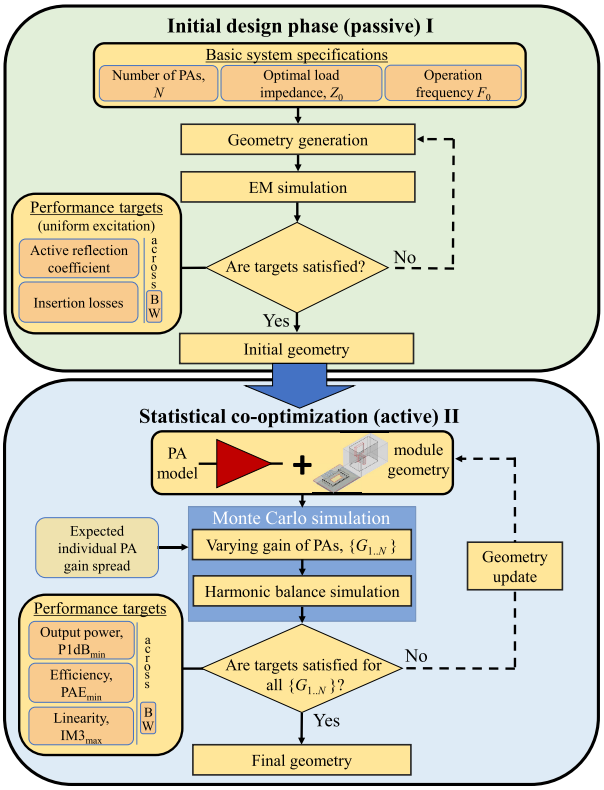

FIGURE 4. A co-design optimization flow for the spatial power combining module.

etched rectangular aperture into the metal WR-28 flange with stepped ridges. Due to the low substrate height and different medium the aperture region becomes very sensitive and hence challenging for assembling. Figure 3 shows the geometry of the designed prototype. The divergent MLs were included in the device under test (DUT) to be able to mount RF connectors to the PCB and to decouple the extended routing of MLs.[1] By exploiting symmetry, a two-port-only calibration kit is sufficient to de-embed most of the effects of the four connectors from the measurement results. The structure employs the RO4350 laminate with thickness 0.254 mm and relative dielectric constant $\varepsilon_r = 3.66$.

As mentioned above, the output power, efficiency, and non-linear distortion are highly dependent on the PA load impedances [15]. These loads can be represented by active reflection coefficients at the combiner input ports:

$$\Gamma_n = \frac{1}{G_n} \sum_{m=1}^{N} G_m S_{nm}, \tag{1}$$

[1]The extended microstrip lines and coaxial connectors can, in typical applications, be eliminated by mounting the MMIC directly onto the PCB. Although such a structure will be more compact it will not affect the conclusions of the present study.

where S_{nm} is the S-parameter from combiner port m to n, while $G_m = A_m e^{-j\phi_m}$ is the complex gain of the m-th PA. The active impedances at the combiner input ports are assumed to be optimal for achieving high output power and efficiency in case of identical PAs (uniform excitation). However, in practice, individual PAs can differ due to the different thermal regimes of each PA and/or due to fabrication uncertainties. Therefore, interfacing PAs with varying and non-equal gains ($G_n \neq G_m | n, m \in \{1 \ldots N\}$) to a non-isolating combiner ($S_{nm}|_{n \neq m} \neq 0$) affects the active impedances at the combiner input ports, and hence, degrades the individual PA performance. Taking the above effects into account, a more holistic design procedure has been proposed (See Fig. 4). It consists of two design phases: initial passive design phase similar to work [14] and statistical co-optimization, which includes large-signal behavior of coupled realistic PAs. In the first phase, an initial module geometry is created based on the initial system specifications, such as the number of PAs, optimum load impedance, and operation frequency. This geometry is numerically optimized under the condition of uniform excitation to satisfy the initial performance goals: active reflection coefficients and insertion loss levels over a certain frequency bandwidth.

In the second design phase, the initially realized geometry is co-optimized in conjunction with a large-signal PA model. Individual PA gains are statically varied using Monte Carlo

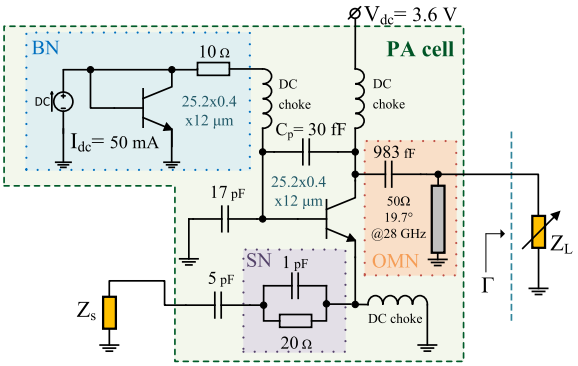

FIGURE 5. Simulated Class-A single-ended common-base output PA stage in SiGe HBT technology. OMN = output matching network, BN = bias network, SN = stability network. An active load sweep is performed.

method in order to emulate a realistic PA gain spread. The performance of such a joint active structure is evaluated in terms of PA metrics: output power, efficiency, linearity. If the performance targets are satisfied for all possible realizations, the final geometry is obtained. Otherwise, the module geometry needs to be updated. The above procedure also allows one to determine the maximum allowable variation of the PA gains.

In the present design an output stage based on conventional single-ended common-base amplifier has been employed (See Fig. 5). The design is implemented in 0.25μm SiGe:C BiCMOS technology [18], which is also the technology used for the quad channel IC in our experimental verification (*cf*. Section 3). SiGe heterojunction bipolar transistors (HBTs) operated in the common-base configuration are widely used at high frequencies due to the higher maximum available power gain and relatively higher output load compared to the common-emitter configuration [19], [20]. The scale of the HBT has been chosen in such a way to operate near peak current density while remaining in safe operation in terms of electro-thermal breakdown [21]. This resulted in a high-voltage HBT with a $0.4 \times 25.2 \times 12$ μm emitter area. A simple biasing network based on the current mirror has been employed, $I_{dc} = 50$ mA corresponds to the class A/B operation point. In order to improve electrical stability at lower frequencies an additional high-pass shunt RC network (20 Ω, 1 pF) has been used. An output matching circuit based on transmission lines has been used in order to match the output stage to 50-Ω load. The capacitor $C_p = 30$ fF represents a typical parasitic layout capacitance. The load-pull simulations have been performed in Keysight ADS using a harmonic balance technique. The simulated PA output power at 1-dB compression point (P1dB) reaches the maximum value of 23.5 dBm and remains above 23 dBm over the entire PA operation bandwidth (26.5–29.5 GHz). The corresponding power efficiency at P1dB point is above 35%. The maximum PA gain of 8.5 dB is observed at 28 GHz.

Figure 6 shows the simulated P1dB output power and efficiency contours at 28 GHz in the load reflection coefficient plane. The clusters of points represent $\Gamma_{1,2}$ of the multi-port power combiner in the presence of normally distributed phase and amplitude deviations representing non-indantical PAs with standard deviation, σ, of 1 dB and 15°, respectivly. As one can see, most of the active load realizations remain within the region of high efficiency and high output power, although for higher σ the cluster of points is more spread.

Another important performance metric of a PA is its linearity. Nonlinear properties of the PA interconnected to the power combining module have been quantified by performing a two-tone test. The relative magnitude of the output third-order intermodulation (IM3) products has been used as a measure of nonlinearity. The IM3 products are the most critical ones for this design since they appear in the operating frequency range. In the performed test, two spectrally pure tones at frequencies f_1 and f_2 are applied to the PA input

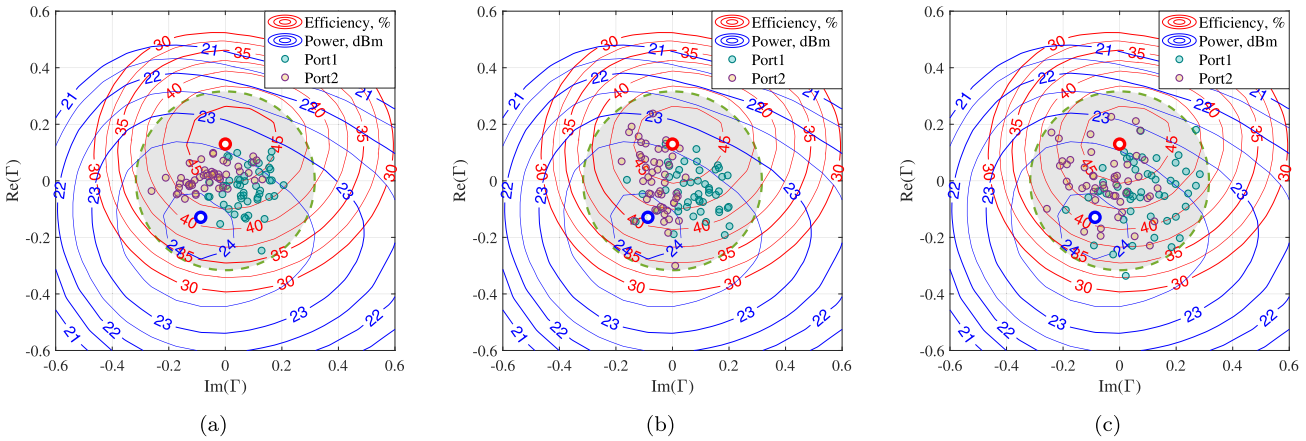

FIGURE 6. Simulated PA P1dB output power (blue) and efficiency (red) contours at 28 GHz in the load reflection coefficient plane. The cluster of points represent $\Gamma_{1,2}$ of the power combining module in the presence of normally distributed: (a) Phase errors with $\mu = 0°$ and $\sigma = 15°$; (b) Amplitude errors with $\mu = 0$ dB and $\sigma = 1$ dB; (c) Both amplitude and phase errors. The colored regions indicate $|\Gamma_{1,2}| \leq -10$ dB.

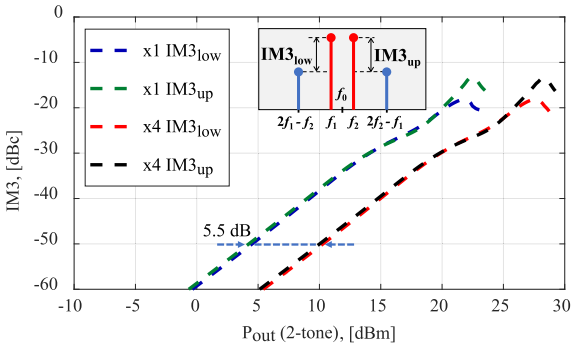

FIGURE 7. Simulated output third-order intermodulation products relative to the corresponding fundamental tones as a function of the two-tone output power in case of a single PA (×1) and the combined PA (×4). The testing was carried out at $f_0 = 28$ GHz with two-tone spacing of $\Delta f = 0.1$ GHz.

port. The tones are centered around the center frequency, $f_0 = 28$ GHz, and separated by $\Delta f = 0.1$ GHz, such that $f_1 = f_0 - \Delta f$ and $f_2 = f_0 + \Delta f$. A large input signal drives the PA into its nonlinear operating range. As a result, IM3 products appear in the output signal at frequincies $2f_1 - f_2$ and $2f_2 - f_1$. Figure 7 shows the magnitude of the output IM3 products relative to the corresponding fundamental tones as a function of the two-tone input power for a single PA (curve ×1) and the combined PA (×4). As expected, operating at higher output power levels leads to a significant increase in the relative magnitude of IM3 components. Asymmetry of the magnitude of the upper and lower IM3 products is similar for both considered cases and indicates the memory effects in the nonlinear transfer function of the PA. The IM3 curves for the combined PA are 5.5 dB shifted compared to the single PA case whereas their shapes are the same for both configurations. The latter confirms that the module itself has no effect on linearity. However, the output impedance mismatch caused by non-equal PA gains might affect the linearity of the combined PA. Figure 8 shows the relative output IM3 products in the load reflection coefficient plane

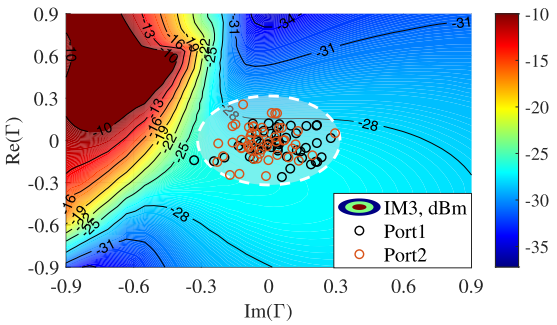

FIGURE 8. The output third-order intermodulation product relative to the fundamental tone in the load reflection coefficient plane. The testing was carried out at $f_0 = 28$ GHz with two-tone spacing of $\Delta f = 0.1$ GHz, $P_{in} = 10$ dBm. The cluster of points represent $\Gamma_{1,2}$ of the power combining module in presence of normally distributed phase and amplitude deviations with $\sigma = 1$ dB and 15° respectivly. The colored regions indicate $|\Gamma_{1,2}| \leq -10$ dB.

for a single PA. The testing is carried out at $f_0 = 28$ GHz with $\Delta f = 0.1$ GHz, $P_{in} = 10$ dBm. The cluster of points represents $\Gamma_{1,2}$ of the power combining module in the presence of normally distributed phase and amplitude with standard deviation, σ, of 1 dB and 15°, respectively. As one can see, most of the active load realizations correspond to the same relative IM3 level (−28 dBc), which indicates a negligible effect of the load mismatch on the combined PA linearity. The conclusions are the same for different input power levels, P_{in}, and these results have therefore been omitted. A combined PA could be considered as a single unit with a nonlinear transfer function. Therefore, conventional techniques such as feedback, feed forward, analog and digital pre-distortion are applicable for its linearization [22].

This study has been used to determine the PA requirements in terms of the maximum allowable relative difference of the phase and amplitude. The results show that good performance (relative output power reduction ≤ 1 dB) can be expected as long as PA gain variations remain within ±15° for the phase and ±1 dB for the amplitude. The corresponding optimum combiner design parameters (in mm) are shown in Table 2.

TABLE 2. The optimum design parameters, as shown in Figure 3.

L_w	W_w	G_s	L_s	W_s	W_{r1}	L_{r1}	W_{r2}	L_{r2}	H
3.56	7.11	0.77	1.53	3.40	0.71	1.72	2.69	0.53	6.00
w_1	w_2	g_1	g_2	s_0	s	d	W	h_1	L
0.79	0.43	0.42	0.38	0.25	0.63	0.3	5.79	2.32	1.21
l_1	l_2	l_3	l_4	l_5	l_6	α	h_2		
0.74	2.00	1.54	5.00	1.9	0.63	135°	2.71		

A non-uniform input port excitation also causes the higher-order modes in the SIW-based cavity to be excited with different amplitudes. Higher-order modes at the antenna side of the discontinuity radiate out directly if these are propagating modes and thus affect the radiation pattern shape when excited strongly. If higher-order modes are evanescent, they will store different amounts of reactive energy at the transition depending upon their excitation, which in turn affects the PA matching as well as the PA gain, efficiency and output power, also for the dominant propagating mode. The latter effect is already modeled by the existing dominant mode S-parameter matrix. Finally, the amplitude level of the higher-order evanescent modes could still be significant in the closely located output port. Interfacing a radiation element supporting the propagation of higher-order modes to such a port might degrade the radiation pattern shape. Thus it is important to investigate the aperture modal content and their excitation profile in the presence of a non-uniform excitation.

An H-plane flared horn supporting the propagation of TE_{10}-TE_{30} modes has been simulated in conjunction with the proposed power combining module in the presence of randomly distributed phase errors with maximum deviation $\Delta\phi$ at 30 GHz (See Fig. 9). The realizations corresponding to the lowest TE_{10} amplitude (worst-case scenario) are given

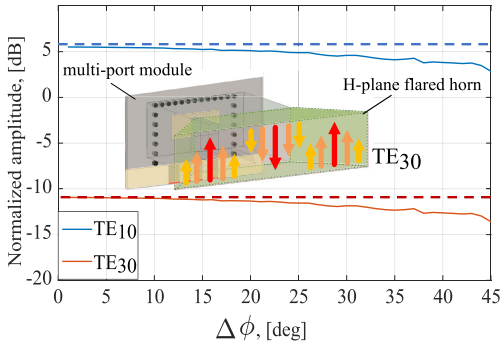

FIGURE 9. Simulated amplitudes of the propagating TE_{10} (blue) and TE_{30} (red) modes in the aperture of a H-plane flared horn with multi-port excitation in the presence of randomly distributed phase errors with maximum deviation $\Delta\phi$. The realizations corresponding the lowest TE_{10} amplitude are given for each $\Delta\phi$. Dashed lines show corresponding mode levels in case of a single-mode wave-port excitation at the horn base.

for each $\Delta\phi$. Dashed lines show corresponding mode levels in the case of a single wave-port excitation. Due to the symmetry of the structure, the TE_{20} mode level is negligible and this result has therefore been omitted. As one can see, increasing $\Delta\phi$ does not increase the TE_{30} mode level, in fact, the relative level to that of the main TE_{10} mode remains the same. Consequently, the total aperture field distribution is not a function of $\Delta\phi$, which confirms the pattern shape sustainability over a range of phase excitations.

III. MEASUREMENT RESULTS

The designed passive prototype has four 50-Ω coaxial ports for testing with a standard VNA and a single WR-28 antenna interface (See the photos in Fig. 10).

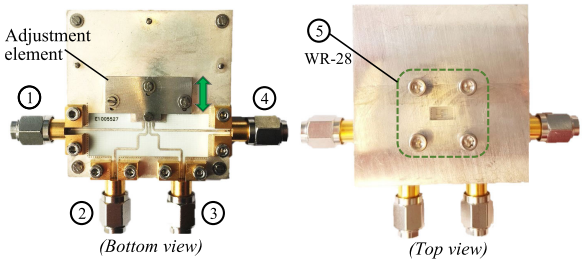

FIGURE 10. Fabricated spatial power combining module prototype.

The prototype is formed by stacking a standard double-sided PCB on the aluminium WG flange, which contains embedded ridges. As discussed in the previous section, the region between the etched aperture and the bottom ridge is very sensitive to fabrication tolerances, and an extra adjustment element was, therefore, developed. It constitutes a movable metal plate with a trimming screw, which can be used to control pressure contact between the PCB and the aluminium flange. The top side of the flange has a standard WR-28 interface, which can also be used as an open-ended WG radiating element. The stack has on overall size of approximately 46 × 46 × 6 mm.

A. INPUT IMPEDANCE MATCHING

The measured and simulated WR-28 port reflection coefficients are shown in Figure 11 with the 50-Ω terminated coaxial ports. It is seen that $S_{55}^{WR-28} < -14$ dB from 24.5–37.8 GHz. The measured active reflection coefficients of the symmetric 50-Ω ports are shown in Figure 12. The active reflection coefficients are calculated from the measured 5 × 5 S-matrix assuming the uniform excitation scenario. The obtained $|\Gamma_1|$ and $|\Gamma_2| < -13$ dB in the desired frequency range, and remain < -10 dB for frequencies in the range 24.5–37.8 GHz. This corresponds to a 42% bandwidth. All curves are close to each other and in good agreement with the simulations shown by black dashed lines. Visible ripples are attributed to the connector interfaces and bent MLs, which cannot be completely de-embedded by the designed two-port TRL calibration kit, since the ports are slightly different in practice. The measured and simulated WR-28 port reflection

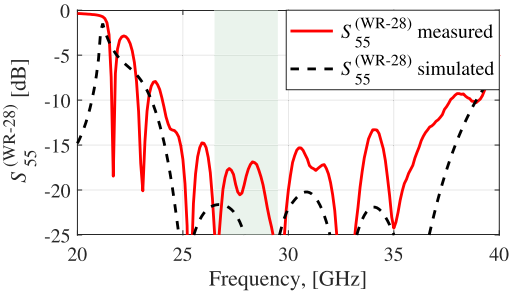

FIGURE 11. Measured (solid) and simulated (dashed) reflection coefficient of WR-28 port (coaxial ports are terminated), as shown in Fig. 10. The colored region shows the operation band of PAs.

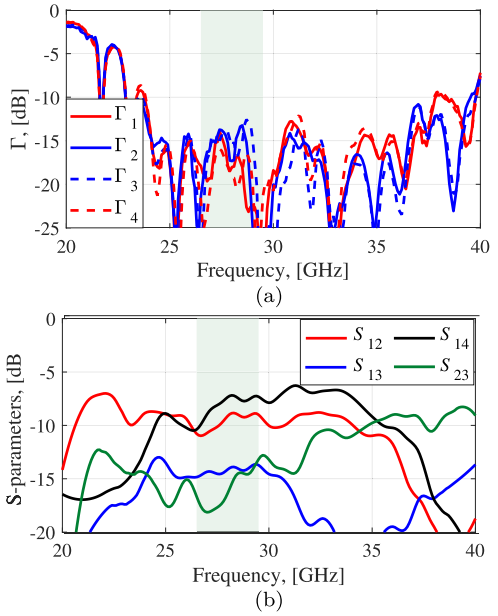

FIGURE 12. Measured: (a) Active reflection coefficients of the 50-Ω microstrip ports of the prototype (including effect of connectors), as shown in Fig. 10 (WR-28 port is terminated); (b) Mutual coupling coefficients between the input ports. The colored region shows the operation band of PAs.

coefficients do not exceed −15 dB and −20 dB, respectively. The observed difference between measurements and simulations is mainly attributed to the connector interfaces and bent MLs which cannot be completely de-embedded by the designed two-port ML TRL calibration kit, since in practice the ports are slightly different. Figure 12 (b) shows the coupling coefficients between the 50-Ω input ports. As one can see, the coupling between the edge ports ($|S_{14}|$) reaches −7 dB level, whereas the coupling between port 1 and port 3 ($|S_{13}|$) is below −14 dB over the entire PA operation frequency range. The relatively high $|S_{14}|$ does not significantly affects the individual PA performance (*cf* Section 2) and mainly attributes to the coupling between the ports within SIW modes.

B. RADIATION PATTERN

The radiation performance has been investigated in conjunction with a standard gain horn antenna at the desired frequency range.

Figure 13 shows the measured H-plane radiation pattern at 28 GHz that was obtained by combining four embedded element patterns, each of which corresponds to the excitation of one port while terminating the others. As one can see, the relative difference between the measured patterns with the single port and multi-port feeding is negligible (<−35 dB within the angular region of ±20°). This difference is comparable with a relative measurement uncertainty, which increases to −20 dB at larger angles. This fact confirms a good rejection of higher-order propagating modes that, in general, can be excited through asymmetric feeding. The conclusions are the same for the E-plane patterns and these results have therefore been omitted.

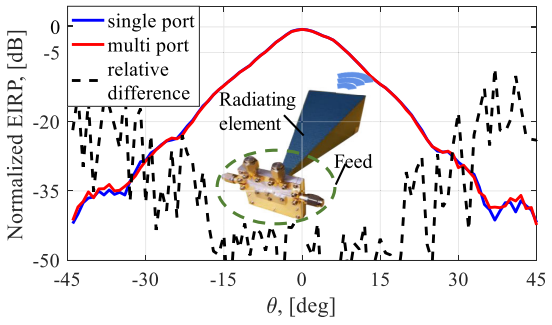

FIGURE 13. Measured H-plane normalized EIRP pattern of the standard gain horn antenna connected to the proposed spatial power combining module (red) and conventional probe-type feed (blue) at 28 GHz. The relative difference is shown by the black dashed line.

C. POWER COMBINING

In order to demonstrate the proposed concept in the presence of the critical effects of realistic power amplifiers, the fabricated power combining module has been interfaced to Class-A/B PAs. The PAs are integrated as a part of a quad-channel beamforming SiGe HBT IC [23], as shown in Figure 14. The beamforming IC has one input and four output RF branches operating in the 26.5–29.5 GHz frequency band.

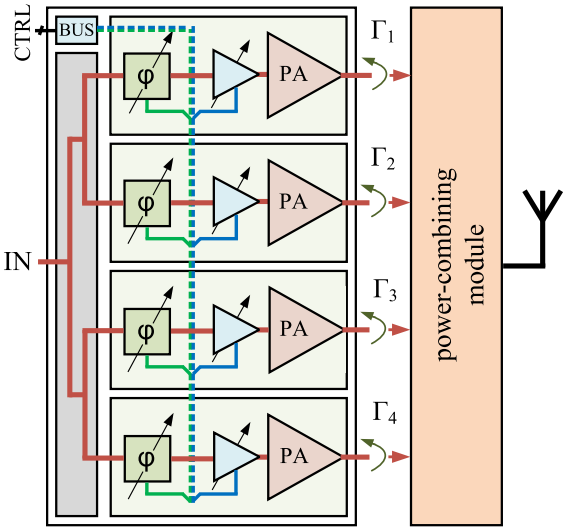

FIGURE 14. Architecture of the quad-channel beamforming SiGe HBT IC in connection with power combining module.

The beamforming IC input and output ports have a 50-Ω nominal impedance. The beamforming IC on the evaluation board has been connected to the multi-port combiner by four short coaxial cables. Such connection allows for an extra flexibility during the calibration and measurements. In practical applications the IC can be directly mounted on the same PCB without any cables and routing lines. The gain and phase of each branch can be controlled via a digital interface using a proprietary protocol. The phase and amplitude values have a 6-bit range, which results in ±5.6° and 0.5 dB resolution for the phase and amplitude respectively. This ability has been used to compensate for various lengths of cables between the beamforming IC board and the power combiner. It allows driving the proposed structure with a calibrated equal amplitude and phase distribution, but also to examine the effect of amplitude and phase variations. The efficiency of PAs cannot be measured since the beamformer IC does not have separate biasing pins for the output stage. Figure 15 illustrates the measurement setup.

Figure 16 shows the relative increase of the generated output power of the 4 × PA combined by the proposed module with respect to a single PA over the 24–31 GHz frequency range for different PA operational regimes. The measured results are compared to the EM simulated model, which accounts for dielectric losses. The measured result in the linear regime is close to the simulation, however, the average level is a bit lower due to the losses in the extended routing of the MLs. The dielectric and radiation losses have been estimated based on the HFSS simulated data. At 30 GHz, the total simulated losses of the DUT are

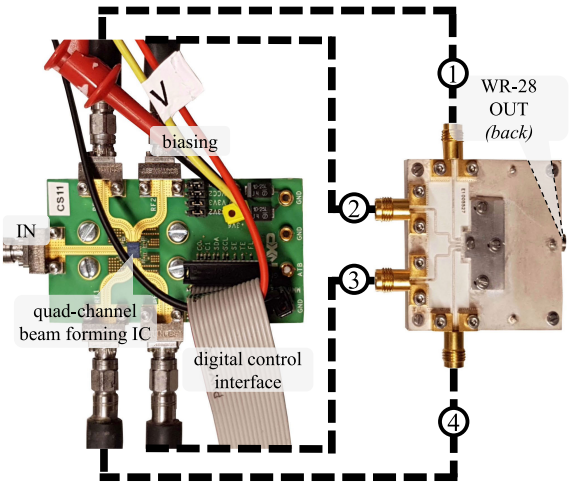

FIGURE 15. Measurement setup for evaluating the power combining module in conjunction with PAs (vector network analyzer and cables are not shown).

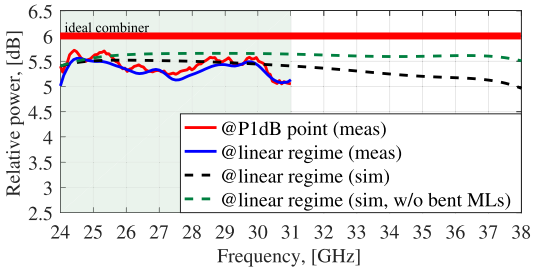

FIGURE 16. Simulated (dashed) and measured (solid) relative increase of the generated output power of the 4 × PA combined by the proposed module, as shown Fig. 3, with respect to a single PA in nonlinear (P1dB point) and linear regime. The colored region shows the operation band of PAs.

0.55 dB, where the contribution of dielectric and radiation losses are 0.19 and 0.36 dB, respectively. Radiation losses are dominant and attributed to the bent MLs, but these can be eliminated through direct MMIC interfacing. The overall expected losses of the proposed spatial power combining module without extended routing lines do not exceed 0.3 dB. Since we are using a parallel power combiner, the losses do not significantly increase with the number of added amplifiers, in contrast to conventional on-chip power combining techniques (See Table 1). There is no considerable difference between the measured relative power increase in the linear and nonlinear regime.

Also, there is a slightly higher (0.3 dB) relative power increase in the nonlinear regime at some frequency points. This is due to the PA dissimilarities, which have not been compensated for in the measurements. Hence, the spatial power combining module does not affect the PA performance over the whole input power range.

Figure 17 shows the measured combined power compared to the output power of each PA versus input power. The input and output powers were normalized to obtain 0 dB gain at the P1dB point. The nonlinear behaviour of the joint

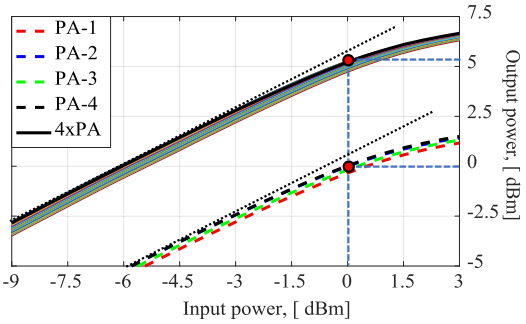

FIGURE 17. Normalized measured output power versus input power for single PAs (dashed) and after combination with proposed module (solid) at 28 GHz. The set of curves shows measured performance reduction in the presence of ±15° phase variation.

PA and power combining module is similar to a single PA. The performance reduction in the presence of phase deviations has been investigated by manually adjusting the phase shift for each beamformer IC branch. The measured set of curves (semitransparent) correspond to ±15° phase variation. As one can see, in the worst scenario the output power decrease is less than 1 dB, which is in good agreement with simulations (See Fig. 6).

IV. CONCLUSION

The joint optimization procedure of a spatial power combining module has been proposed and proven necessary to account for the critical effects of coupled PAs and to ultimately improve the large-signal performance of the combined PA. A class-A single-ended common-base output PA stage in SiGe HBT technology has been employed in the present design. The developed power combining module facilitates efficient mm-wave power generation over 42% bandwidth (24.5–37.8 GHz) where the total power loss due to this module is ≤0.5 dB in simulations and ≤0.7 dB in measurements. The performed statistical study shows that good performance (relative output power reduction ≤ 1 dB) can be expected as long as PA gain variations remain within ±15° for the phase and ±1 dB for the amplitude. The corresponding output impedance mismatch caused by non-equal PA gains has a negligible effect on linearity of the combined PA.

To the authors best knowledge, this is the first experimental demonstration of a compact parallel power combiner with optimal excitation of the SIW-based cavity modes through strongly-coupled microstrip lines. The increase of the total generated output power in the nonlinear regime of PAs @P1dB remains virtually constant (5.5 dB for 4 × PA). The over-the-air tests confirm that the antenna pattern shape is stable with negligible degradation effects due to multi-port excitation. The low loss and wideband properties of the proposed solution is expected to play an important role in efficient high power wideband mm-wave transmitters.

ACKNOWLEDGMENT

The authors wish to thank Dr. Oleg Iupikov for assisting with the measurements.

REFERENCES

[1] J.-S. Rieh, B. Jagannathan, D. R. Greenberg, M. Meghelli, A. Rylyakov, F. Guarin, Z. Yang, D. C. Ahlgren, G. Freeman, P. Cottrell, and D. Harame, "SiGe heterojunction bipolar transistors and circuits toward terahertz communication applications," *IEEE Trans. Microw. Theory Techn.*, vol. 52, no. 10, pp. 2390–2408, Oct. 2004.

[2] J. Edstam, J. Hansryd, S. Carpenter (Feb. 2017). *Ericsson Technology Review: The New Microwave Backhaul Frontier*. [Online]. Available: https://www.ericsson.com/assets/local/publications/ericsson-technology-review/docs/2017/etr-beyond-100ghz.pdf

[3] K. H. An, O. Lee, H. Kim, D. H. Lee, J. Han, K. S. Yang, Y. Kim, J. J. Chang, W. Woo, C.-H. Lee, H. Kim, and J. Laskar, "Power-combining transformer techniques for fully-integrated CMOS power amplifiers," *IEEE J. Solid-State Circuits*, vol. 43, no. 5, pp. 1064–1075, May 2008.

[4] K. Kim and C. Nguyen, "A V-Band power amplifier with integrated Wilkinson power dividers-combiners and transformers in 0.18-μ m SiGe BiCMOS," *IEEE Trans. Circuits Syst. II, Exp. Briefs*, vol. 66, no. 3, pp. 337–341, Mar. 2019.

[5] Q. J. Gu, Z. Xu, and M.-C.-F. Chang, "Two-way current-combining W-band power amplifier in 65-nm CMOS," *IEEE Trans. Microw. Theory Techn.*, vol. 60, no. 5, pp. 1365–1374, May 2012.

[6] J. Xia, X.-H. Fang, and S. Boumaiza, "60-GHz power amplifier in 45-nm SOI-CMOS using stacked transformer-based parallel power combiner," *IEEE Microw. Wireless Compon. Lett.*, vol. 28, no. 8, pp. 711–713, Aug. 2018.

[7] M. P. DeLisio and R. A. York, "Quasi-optical and spatial power combining," *IEEE Trans. Microw. Theory Techn.*, vol. 50, no. 3, pp. 929–936, Mar. 2002.

[8] J.-G. Kim and G. M. Rebeiz, "Miniature four-way and two-way 24 GHz wilkinson power dividers in 0.13 μm CMOS," *IEEE Microw. Wireless Compon. Lett.*, vol. 17, no. 9, pp. 658–660, Sep. 2007.

[9] C. Wang, H. Wu, and C. C. Tzuang, "A miniaturized power combiner for compact design of CMOS phase shifter at K-band," in *IEEE MTT-S Int. Microw. Symp. Dig.*, May 2010, pp. 121–124.

[10] M.-J. Chiang, H.-S. Wu, and C.-K.-C. Tzuang, "Ka-band CMOS hybrids miniaturization incorporating multilayer synthetic quasi-TEM transmission lines," in *Proc. 38th Eur. Microw. Conf.*, Oct. 2008, pp. 329–332.

[11] T. Chi, S. Li, J. S. Park, and H. Wang, "A multifeed antenna for high-efficiency on-antenna power combining," *IEEE Trans. Antennas Propag.*, vol. 65, no. 12, pp. 6937–6951, Dec. 2017.

[12] B. Goettel, P. Pahl, C. Kutschker, S. Malz, U. R. Pfeiffer, and T. Zwick, "Active multiple feed on-chip antennas with efficient in-antenna power combining operating at 200–320 GHz," *IEEE Trans. Antennas Propag.*, vol. 65, no. 2, pp. 416–423, Feb. 2017.

[13] S. M. Bowers and A. Hajimiri, "Multi-port driven radiators," *IEEE Trans. Microw. Theory Techn.*, vol. 61, no. 12, pp. 4428–4441, Dec. 2013.

[14] A. Roev, R. Maaskant, A. Hook, and M. Ivashina, "Wideband mm-Wave transition between a coupled microstrip line array and SIW for high-power generation MMICs," *IEEE Microw. Wireless Compon. Lett.*, vol. 28, no. 10, pp. 867–869, Oct. 2018.

[15] F. M. Barradas, P. M. Tome, J. M. Gomes, T. R. Cunha, P. M. Cabral, and J. C. Pedro, "Power, linearity, and efficiency prediction for MIMO arrays with antenna coupling," *IEEE Trans. Microw. Theory Techn.*, vol. 65, no. 12, pp. 5284–5297, Dec. 2017.

[16] J. Staudinger, "Multiharmonic load termination effects on GaAs MESFET power amplifiers," *Microw. J.*, vol. 39, no. 1, pp. 66–77, Apr. 1996.

[17] T. Li and W. Dou, "A wideband right-angle transition between thin substrate integrated waveguide and rectangular waveguide based on multi-section structure," *Int. J. Microw. Wireless Technol.*, vol. 8, no. 2, pp. 185–191, Mar. 2016.

[18] W. D. van Noort, A. Rodriguez, H. Sun, F. Zaato, N. Zhang, T. Nesheiwat, F. Neuilly, J. Melai, and E. Hijzen, "BiCMOS technology improvements for microwave application," in *Proc. IEEE Bipolar/BiCMOS Circuits Technol. Meeting*, Oct. 2008, pp. 93–96.

[19] Z. Ma and N. Jiang, "On the operation configuration of SiGe HBTs based on power gain analysis," *IEEE Trans. Electron Devices*, vol. 52, no. 2, pp. 248–255, Feb. 2005.

[20] Z. Ma, N. Jiang, G. Wang, H. Li, and G. Qin, "An omni-directional comparison between common-emitter and common-base SiGe HBTs," in *Proc. 8th Int. Conf. Solid-State Integr. Circuit Technol. Proc.*, Oct. 2006, pp. 166–169.

[21] T. Vanhoucke and G. A. M. Hurkx, "Unilfied electro-thermal stability criterion for bipolar transistors," in *Proc. Bipolar/BiCMOS Circuits Technol. Meeting*, Oct. 2005, pp. 37–40.

[22] A. Katz, "Linearization: Reducing distortion in power amplifiers," *IEEE Microw. Mag.*, vol. 2, no. 4, pp. 37–49, Dec. 2001.

[23] Y. Pei, "Silicon-based Ka-band reconfigurable phased-array transmitter," Ph.D. dissertation, Dept. Elect. Eng., Eindhoven Univ. Technol., Eindhoven, The Netherlands, Sep. 2016.

ARTEM ROEV (Member, IEEE) received the B.Sc. and M.Sc. degrees in technical physics from the Peter the Great St. Petersburg Polytechnic University, Saint Petersburg, Russia, in 2014 and 2016, respectively.

From 2014 to 2016, he was an Electronics Engineer with the Institute of Applied Astronomy, Russian Academy of Sciences (IAA-RAS). He is currently pursuing the double Ph.D. degree with the Chalmers University of Technology, Sweden, and the Eindhoven University of Technology, The Netherlands, under the European Innovative Training Network "SILIKA: 5G mm-Wave Array Antenna Systems." His current research interests include the design of passive and active components for integrated high-power antenna array transmitters. In particular, his focus is on SiGe BiCMOS technologies for mm-wave applications.

PARASTOO TAGHIKHANI received the B.Sc. and M.Sc. degrees in electrical engineering and telecommunication from Shahed University, Tehran, Iran, in 2008 and 2011, respectively. She is currently pursuing the Ph.D. degree with the Department of Microtechnology and Nanoscience (MC2), Chalmers University.

Her current research interests include modeling of the hybrid beamforming transmitters for MIMO systems to predict nonlinear distortion and radiation pattern and thermal network extraction for electro-thermal analysis of active circuits.

ROB MAASKANT (Senior Member, IEEE) received the M.Sc. and Ph.D. degree *(cum laude)* in electrical engineering from the Eindhoven University of Technology (TU/e), Eindhoven, The Netherlands, in 2003 and 2010, respectively.

He was employed as an Antenna Researcher with the Netherlands Institute for Radio Astronomy (ASTRON), Dwingeloo, The Netherlands, from 2002 to 2010. Since 2010, he has been with the Antenna Group, Electrical Engineering Department, Chalmers University of Technology, Sweden, where he held a postdoctoral research and assistant professor positions. He is currently an Associate Professor with Chalmers and TU/e. The latter position is owing to a five-year Vidi grant from the Dutch Research Council. He is the primary author of the CAESAR software; an advanced integral-equation-based solver for the analysis of large antenna array systems. His current research interest includes the analysis and design of integrated antenna array systems for future wireless applications. He has served the AP Community as an Associate Editor for the IEEE TRANSACTIONS ON ANTENNAS AND PROPAGATION and the IEEE ANTENNAS AND WIRELESS PROPAGATION LETTERS. He is in the Editorial Board of a unique open-access journal: *Forum for Electromagnetic Research Methods and Application Technologies (FERMAT)*.

CHRISTIAN FAGER (Senior Member, IEEE) received the Ph.D. degree from the Chalmers University of Technology, Sweden, in 2003.

Since 2019, he has been a Full Professor with the Microwave Electronics Laboratory, Chalmers University of Technology. He has authored or coauthored more than 130 publications in international journals and conferences. His research interests include the area of energy efficient and linear transmitters for future wireless communication systems. He received the Best Student Paper Award at the IEEE International Microwave Symposium, in 2003. He serves as a member of the Technical Coordinating Committee on Wireless Communication of the IEEE Microwave Theory and Techniques Society, and is currently an Associate Editor of *IEEE Microwave Magazine* and IEEE MICROWAVE AND WIRELESS COMPONENTS LETTERS.

MARIANNA V. IVASHINA (Senior Member, IEEE) received the Ph.D. degree in electrical engineering from Sevastopol National Technical University (SNTU), Ukraine, in 2001. From 2001 to 2010, she was with the Netherlands Institute for Radio Astronomy (ASTRON), where she carried out research on innovative phased array technologies for future radio telescopes, such as the Square Kilometer Array (SKA). She is currently a Professor in antenna systems with the Chalmers University of Technology, Gothenburg, Sweden. Her research interests include wideband receiving arrays, antenna system modeling techniques, receiver noise characterization, signal processing for phased arrays, and radio astronomy. She has published extensively on the above topics, having authored/coauthored over 120 journal and conference papers. She is currently an Associate Editor of the IEEE TRANSACTIONS ON ANTENNAS AND PROPAGATION.